Computational analysis on native and extrinsic point defects in YAG using the metaGGA SCAN method

William Lafargue-Dit-Hauret, Mathieu Allix, Bruno Viana, Stéphane Jobic, Camille Latouche

Computational analysis on native and extrinsic point defects in YAG using the metaGGA SCAN method

William Lafargue-Dit-Hauret[1], Mathieu Allix[2], Bruno Viana[3], Stéphane Jobic[1*] and Camille Latouche[1*]

[1]Nantes Université, CNRS, Institut des Matériaux de Nantes Jean Rouxel, IMN, F-44000, Nantes, France.
[2]Conditions Extrêmes et Matériaux: Haute Température et Irradiation, CEMHTI, UPR 3079, CNRS, Université Orléans, Orléans, 45071, France.
[3]PSL Research University Chimie ParisTech, IRCP, CNRS, Paris, 75005, France.

*Corresponding author(s). E-mail(s): stephane.jobic@cnrs-imn.fr; camille.latouche@cnrs-imn.fr;

Abstract

We report on the computational study of point defects in the well-known $Y_3Al_5O_{12}$ (YAG) compound. DFT SCAN and SCAN+U calculations were used to access the electronic properties of the material taking into account both native defects and two substituting dopants, namely Ce and Cr. Defect formation enthalpies and defect concentrations were estimated for different synthesis conditions corresponding to extreme and intermediate limits of the stability diagram of YAG. We demonstrate that $\boldsymbol{Y_{Al}}$ antisites at Al octahedral position cannot be avoided whatever the synthesis atmosphere. As expected, $\boldsymbol{V_O}$ oxygen vacancies are easily formed under reducing atmospheres. Moreover, we have notably show that the formal Ce^{3+}/Ce^{4+} charge transition

level is getting closer to the experimental value for a Hubbard correction $\boldsymbol{U_{eff}}$ of 5 eV. Last, the electron traps associated to the reduction of Cr^{3+} into Cr^{2+} species were identified near the conduction band.

Keywords: yttrium-aluminum garnet, YAG, point defects, Density Functional Theory

Graphical Abstract.

1 Introduction

The yttrium-aluminum garnet $Y_3Al_5O_{12}$, commonly abbreviated YAG, is a well-known host material largely used since many decades in efficient and powerful optical technologies. Hence, as early 70s, a neodymium-doped yttrium aluminum garnet (Nd:YAG) laser crystal was developed and widely adopted due to its superior laser characteristics and high thermal conductivity. Formally, the natural visible range of transparency of undoped YAG due to a wide band gap of ∼6.5 eV [1, 2] enables the triggering of attractive optical properties for industrial purposes by introducing dopants such as rare-earth RE^{3+}. Indeed, the garnet crystal structure allows easy incorporation of trivalent cations such as transition metals TM^{3+} or RE^{3+} species in place of Al or Y sites, respectively [3]. The direct consequence of the presence of these intentionally incorporated dopants is the appearance of defect levels which may lie within the band gap of the ideal YAG material [4]. Depending on the nature of dopants, the position of inserted defect electronic states with respect to the top of the valence band (or Valence Band Maximum, VBM) and the bottom of the conduction band (or Conduction Band Minimum, CBM) will change, possibly affecting the overall optical properties, *i.e.* the light yield, the luminescence spectra and/or the time dependency of the luminescence phenomenon (*e.g.* fluorescence *vs* persistent luminescence and scintillation). Thus, the control and characterization of these defects is of prior importance and paves the way to the engineering of new optical devices.

Nd^{3+}, Er^{3+} and Ho^{3+} doped YAG crystals have been developed for solid state lasers during the last five decades [5–8], while Ce-doped YAG is widely used for lighting in white LEDs [9, 10]. Intensive experimental and theoretical investigations have been devoted to getting deep insights into electronic transitions and to improve constantly the luminescence properties of this latter

[11–13]. In that context, Ueda *et al.* notably found that the concomitant presence of Cr^{3+} and Ga^{3+} was detrimental to fluorescence since they significantly increase the persistent luminescence of YAG:Ce^{3+} by simultaneously generating electron traps and decreasing the CBM position, respectively [14, 15]. This point will be discussed in the last part of the paper.

Moreover, despite computational efforts to dissect the electronic properties of cerium- and chromium-based defects [16–20], some important information such as the impact of synthesis conditions on defect formation energies and the position of charge transition levels (independent of the synthesis conditions) are still lacking to our knowledge. Also, surprisingly, even though many experimental data have been published on the subject, no exhaustive theoretical study gathering results on intrinsic and extrinsic defects in YAG is available yet. Herein, we propose to perform *ab initio* investigations on native point defects and substitutions involving cerium and chromium dopants in YAG.

2 Methods

2.1 Crystal structure

The YAG material crystallizes in the $Ia\bar{3}d$ cubic space group (Z = 8) represented in Figure 1. Yttrium atoms are located in a 24*c* site and are surrounded by eight neighboring O atoms defining [YO_8] environments. Aluminum atoms are found at a 24*d* site for the tetrahedral [AlO_4] environment ($Al(T_d)$), and at a 16*a* site for the octahedral [AlO_6] environment ($Al(O_h)$). The tetracoordinated oxygen atoms are located at a 96*h* site and are surrounded by two Al ($Al(O_h)$ and $Al(T_d)$), and two Y atoms in a pseudo tetrahedral coordination.

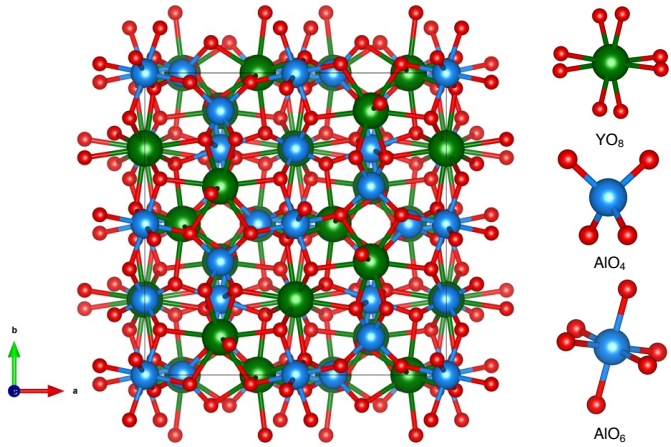

Fig. 1 Crystallographic structure of YAG. Y, Al and O atoms are depicted by green, blue and red spheres, respectively. [YO_8], [AlO_4] and [AlO_6] environments are also evidenced.

2.2 First-principles calculations

Density functional theory (DFT) simulations have been performed using the PAW method as implemented within the VASP code [21–23]. A cutoff energy of 500 eV was considered to set the plane wave basis expansion. The SCAN [24] functional was used for the description of the exchange-correlation term, and the following electronic valence configurations were chosen: $4s^2 4p^6 5s^1 4d^2$ for Y, $3s^2 3p^1$ for Al, $2s^2 2p^4$ for O, $5s^2 5p^6 6s^2 5d^1 4f^1$ for Ce, $3p^6 4s^1 3d^5$ for Cr. Full geometry relaxations have been carried out on the 80 atoms cell considering a 10×10×10 Γ-centered k-points mesh and until the norm of atomic forces was under 0.005 eV/Å. This led to a cell parameter $a = 11.990$ Å once transcribed in the regular I setting, in great agreement with the experimental data [25] reported at 12.000(4) Å. This highlights the potential of this functional to get reliable crystallographic structures. Accurate energy calculations have been performed to estimate the electronic band gap with a 12×12×12 Γ-centered k-mesh. The band gap was found to be 5.08 eV, underestimating the experimental optical value of 6.3-6.7 eV [1, 2] and the PBE0 estimation of

6.8 eV [26]. To overcome the issue of semi-local functionals to estimate accurate electronic band gaps, we used the PBE0 hybrid functional [27] on top of the fully optimized SCAN structure with a 2×2×2 Γ-centered k-mesh for the description of the first Brillouin zone. We found E_g(PBE0@SCAN) = 6.90 eV, which follows the general trend expected for hybrid functionals [28]. We chose the PBE0 results to correct band edges of the host compound in the following of our investigations.

2.3 Defect study

The point defect investigation was done based on the conventional cubic unit cell containing 160 atoms. Formally, single defects were assumed sufficiently diluted in the host matrix, allowing to neglect the interactions with periodic boundary images as well as the minor distortions suffered by the crystal cell. Atomic positions were allowed to accommodate the presence of the defect by relaxing until their forces were smaller than 0.01 eV/Å. Geometry optimizations and accurate energy calculations were performed using a 3×3×3 Γ-centered k-mesh. Regarding the dopants, the cerium and chromium atoms present d and f valence electrons, poorly described by GGA functionals. Previous SCAN studies reported that an Hubbard correction is required for correcting Ce-4f orbitals, and none for Cr-3d states [29, 30]. Following their conclusions, no correction was applied for Cr-3d orbitals and we varied the effective Hubbard term from 2 to 5 eV for the Ce-4f orbitals [31].

All the following defect post-treatments were performed using the PyDEF code [32, 33]. For a point defect D at the charge state q (the relative charge state with respect to the native charge), the defect formation enthalpy (DFE) $\Delta_f H^{D,q}$ is calculated based on the following expression:

$$\Delta_f H^{D,q}\left(\mu_{E_F}\right) = E_{tot}^{D,q} - E_{tot}^{host} + \sum_i n_i \mu_i + q\left(E_{VBM}^{host} + \mu_{E_F}\right) + \tau\left(D,q\right) \quad (1)$$

where $E_{tot}^{D,q}$ is the total DFT energy of the faulted large cell, E_{tot}^{host} is the total DFT energy of the host structure, n_i corresponds to the number of added atoms for the i^{th} species added (n_i ¡ 0) or removed (n_i ¿ 0) from the perfect material, μ_i is the chemical potential of the i^{th} species, μ_{E_F} is the potential of the electron reservoir, E_{VBM}^{host} is the energy associated to the valence band maximum (VBM) of the ideal cell, and τ includes multiple corrections on spurious effects which are detailed in SI Section I.

For a given defect, the Fermi level at which two charge states q and q' present identical DFEs corresponds to the charge transition level $\epsilon\left(q/q'\right)$. This thermodynamic quantity is expressed as:

$$\epsilon\left(q/q'\right) = \frac{\Delta_f H^{D,q}\left(\mu_{E_F}=0\right) - \Delta_f H^{D,q'}\left(\mu_{E_F}=0\right)}{q'-q} \quad (2)$$

More concretely, this point represents the thermodynamic equilibrium between the two charge states where both species coexist in equivalent concentrations. The differences in energy between the VBM and the $\epsilon\left(q/q'\right)$ level and the $\epsilon\left(q/q'\right)$ level and the CBM correspond to an acceptor and a donor energy, respectively.

The concentration $n_{D,q}$ of a defect D in a charge state q may be expressed as:

$$n_{D,q}\left(\mu_{E_F}\right) = N_D \cdot exp\left(-\frac{\Delta_f H^{D,q}\left(E_F^{gr}\right)}{k_B T_{gr}}\right) \quad (3)$$

where N_D is the number of accessible sites for the defect D, E_F^{gr} is the Fermi level at the growth temperature T_{gr}, k_B is the Boltzmann constant.

Entropy effects are neglected. The procedure used to estimate the E_F^{gr} and $n_{D,q}$ quantities at a given T_{gr} value is detailed in SI Section II.

3 Results and discussions

3.1 Native point defects

The first step in the estimation of defect formation enthalpies consists in setting the existence domain of the YAG crystal. In the following, we assumed that entropy effects are negligible. Here, the synthesis conditions are driven by the chemical potentials μ_i, associated to the atomic reservoir of atom i during the reaction and which can be expressed as [34]:

$$\mu_i = \mu_i^0 + \Delta\mu_i \tag{4}$$

where μ_i^0 is the standard chemical potential computed as the total DFT energy per formula unit of the reference phase for the element i, and $\Delta\mu_i$ is the deviation induced by the synthesis conditions. Here, the standard references correspond to the hexagonal close-packed elemental yttrium solid (*hcp*-Y), the face-centered cubic elemental aluminum solid (*fcc*-Al) and the dioxygen molecule ($O_{2(g)}$). The thermodynamic stabilities of the YAG compound *vs* growth conditions are defined by the formation enthalpy expressed as:

$$\Delta_f H(Y_3Al_5O_{12}) = 3\Delta\mu_Y + 5\Delta\mu_{Al} + 12\Delta\mu_O \tag{5}$$

In a more practical growth reaction at the industrial scale, the formation of YAG results from the mixing of Y_2O_3 and Al_2O_3 products [13]. Analogously to Equation 5, the formation enthalpy of YAG may depend on the chemical potential deviations of these two binary oxides ($\Delta\mu_{Y_2O_3}$ and $\Delta\mu_{Al_2O_3}$, respectively), resulting in:

$$\Delta_f H(Y_3Al_5O_{12}) = \frac{3}{2}\Delta\mu_{Y_2O_3} + \frac{5}{3}\Delta\mu_{Al_2O_3} \quad (6)$$

where $\Delta\mu_{Y_2O_3} = \mu_{Y_2O_3} - \mu^0_{Y_2O_3}$ and $\Delta\mu_{Al_2O_3} = \mu_{Al_2O_3} - \mu^0_{Al_2O_3}$ with $\mu^0_{Y_2O_3}$ = -94.04 eV and $\mu^0_{Al_2O_3}$ = -51.07 eV, respectively (calculated values). The impact of the surrounding oxygen atmosphere may be recovered by introducing another variable, namely $\Delta\mu_{O_2} = \mu_{O_2} - \mu^0_{O_2}$ with $\mu^0_{O_2}$ = -12.04 eV. In that sense, oxidized (O-rich, *e.g.* in pure oxygen at ambient pressure) synthesis conditions are representative of small negative $\Delta\mu_{O_2}$ values while large negative $\Delta\mu_{O_2}$ values indicate reducing (O-poor, *e.g.* in evacuated sealed silica tube) atmospheres.

Undesired competing phases and precursors residues can be observed during the growth process. One can prevent the possible formation of these compounds by studying the stability phase diagram of the Y_2O_3-Al_2O_3-O_2 system function of the chemical potential deviations. To do so, we conducted a thermodynamic investigation on 11 competitive phases (the exhaustive list phases are given in Table S1) using the procedure established in Ref 35. Figure 2 reports the stability phase diagram of YAG (yellow region), delimited by the formation enthalpy limits of competitive phases represented by colored lines. The extreme synthesis conditions considered during our study are identified by black points, positioned at the intersection of the lines which define the YAG domain frontier.

The stability region for YAG presents a polygonal shape with five corner boundaries, the related coordinates are detailed in the Y-Al-O (elements) and Y_2O_3-Al_2O_3-O_2 (compounds) frames in SI Table S2 and S3, respectively. One may distinguish i) two O-rich limits at the A ($Y_2O_3/O_{2(g)}$) and B ($O_{2(g)}/Al_2O_3$) points, and ii) three O-poor limits at the C (YAl_3/Al_2O_3), D (YAl_2/YAl_3) and E (Y_2O_3/YAl_2) points. Herein, we focused the following

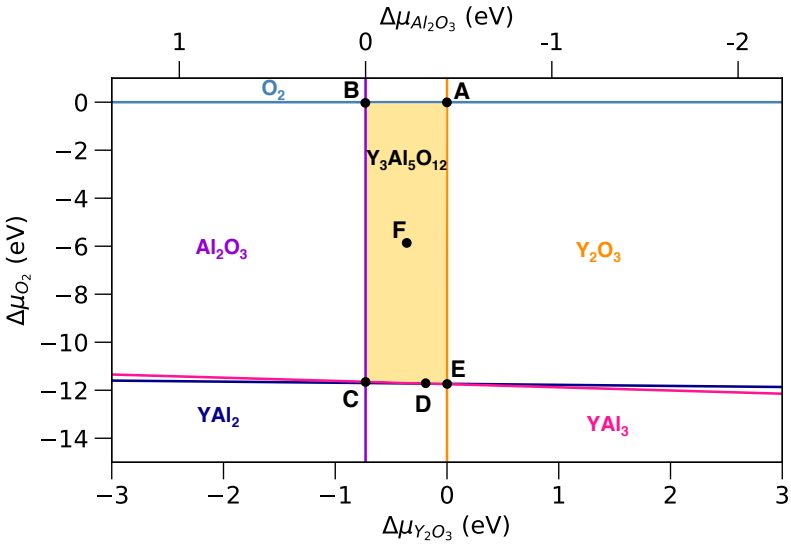

Fig. 2 Stability phase diagram of YAG compound depending on chemical potential deviations in the Y_2O_3-Al_2O_3-O_2 system. Each line corresponds to the formation enthalpy limit with a given competing phase surrounding the existence area of $Y_3Al_5O_{12}$. The exhaustive list of competitive phase is given in SI Table S1. Points of interest are denoted in black and take the following ($\Delta\mu_{Y_2O_3}$, $\Delta\mu_{Al_2O_3}$, $\Delta\mu_{O_2}$) coordinates: A (0.00, -0.44, 0.00), B (-0.73, 0.00, 0.00), C (-0.73, 0.00, -11.65), D (-0.15, -0.35, -11.73), E (0.00, -0.44, -11.73) and F (-0.37, -0.22, -5.85).

part of the paper on the A, B, C and E extreme synthesis conditions, assuming D and E atmospheres are similar at the very first sight since they are very closed in the stability diagram. We also considered the intermediate F point as more representative of common synthesis conditions.

Following, we present the study of DFEs and defect concentrations for intrinsic point defects with the aforementioned chemical potentials. More specifically, we investigated the four possible vacancies of oxygen (V_O), yttrium (V_Y), aluminium ($V_{Al(O_h)}$ in 16a sites and $V_{Al(T_d)}$ in 24d sites) species, as well as three substitutional entities of cations: Al_Y, $Y_{Al(O_h)}$ and $Y_{Al(T_d)}$. Finally, the interstitial defects correspond to cations and anions introduced in 16b and 48g sites, respectively, in the lines of Ref 36 (the initial positions are presented in SI Figure S2). DFEs and related defect concentrations are shown

in Figures 3-5 and Figures 6-8, respectively. The charge transition levels and defect concentrations at T_{gr} = 1850 °C (the growth temperature of garnet in the literature *via* the Czochralski method) are summarized in SI Table S4 and S5, respectively.

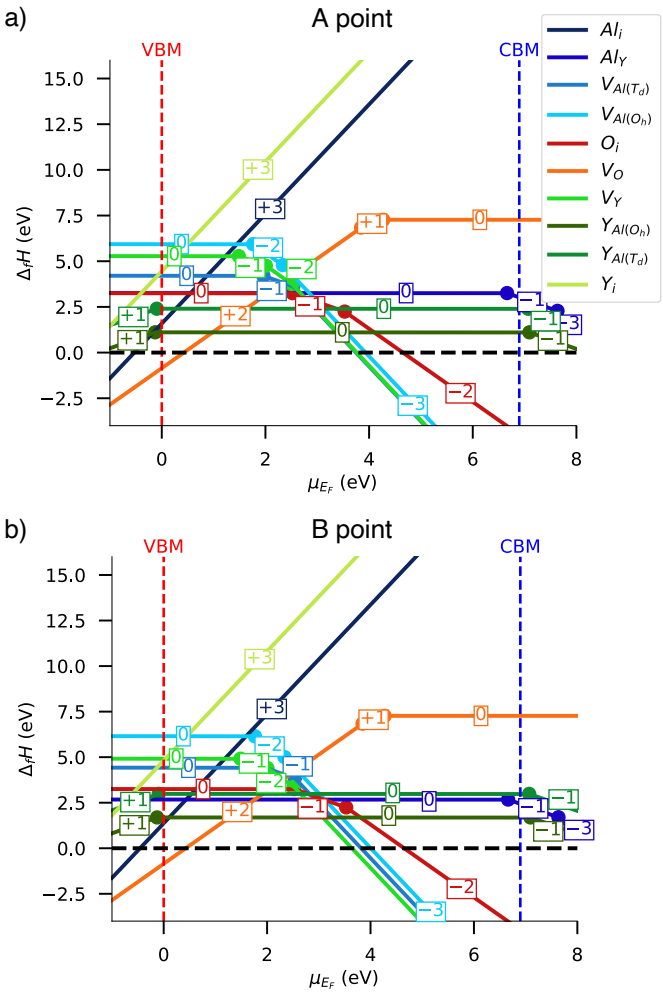

Fig. 3 Defect formation enthalpies *vs* the Fermi level for the O-rich synthesis condition at the a) A and b) B points.

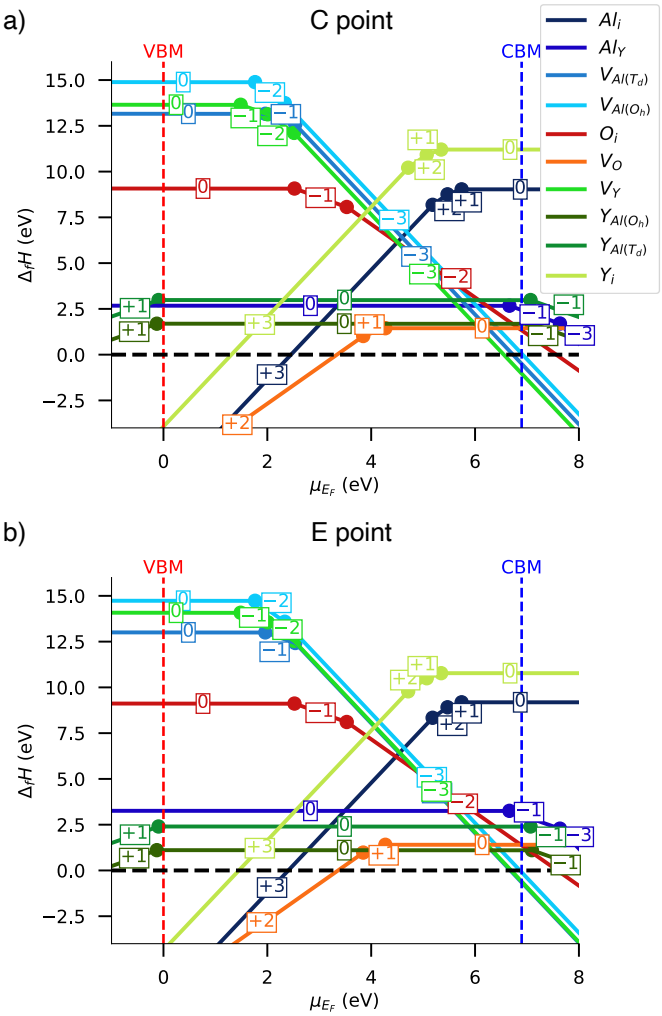

Fig. 4 Defect formation enthalpies *vs* the Fermi level for the O-poor synthesis condition at the a) C and b) E points.

We now detail the thermodynamic changes observed *vs* the synthesis conditions, *i.e.* the $\Delta\mu$ coordinates in the stability domain of Figure 2. At the O-rich A point (see Figure 3a), the region where the DFEs of all intrinsic defects are positive (namely the dopability domain) is set for μ_{E_F} between 0.4 and 3.8 eV by charged V_O and $V_Y/V_{Al(T_d)}$ species, respectively. In this energy window, $Y_{Al(O_h)}$ antisites were found to be the most stable defect species with

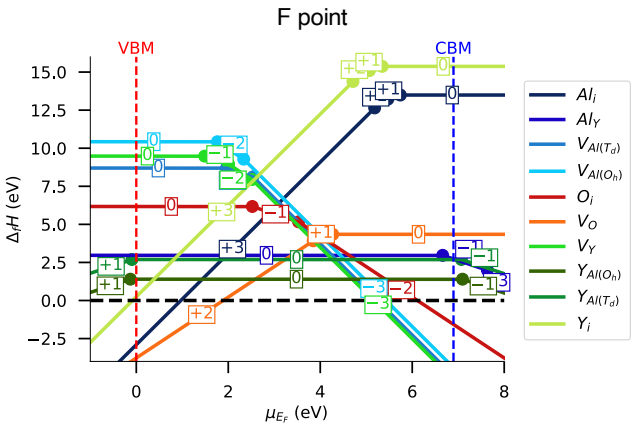

Fig. 5 Defect formation enthalpies *vs* the Fermi level for the O-intermediate synthesis condition at the F point.

DFEs lower than 1.1 eV, *i.e.* twice lower than the substitution occurring at the tetrahedral site ($Y_{Al(T_d)}$) in good agreement with published results [36–40]. Typically for a growth temperature T_{gr} = 1850 °C (growth Fermi level E_F^{gr} calculated at 2.6 eV), the $Y_{Al(O_h)}$ species are more concentrated (2.2×10^{19} cm^{-3}) than the others (see Figure 6a), *i.e.* disfavoured during the synthesis, such as $Y_{Al(T_d)}$ ($\sim10^{16}$) or O_i, $V_{Al(T_d)}$, etc. (found below $\sim10^{15}$ cm^{-3}). At the O-rich B point (E_F^{gr} = 2.6 eV at T_{gr} = 1850 °C, see Figure 3b and Figure 6b), the concentrations of Y-based antisites turn to be lower, *i.e.* $\sim10^{18}$ cm^{-3} and $\sim10^{15}$ cm^{-3} for $Y_{Al(O_h)}$ and $Y_{Al(T_d)}$, respectively, while the concentration of Al_Y increases up to $\sim10^{15}$ cm^{-3} and the one for the others remains more or less constant. This decrease observed for Y_{Al} and increase for Al_Y species follows the chemical intuition with the preferential presence of Y-based species, *i.e.* with lower DFEs, under Y_2O_3-rich (A point) than Y_2O_3-poor (B-point) synthesis conditions, respectively.

Considering the O-poor C point (see Figure 4a), we found that the dopability region is shifted towards high energies and ranges from 3.3 to 6.6 eV, respectively set by oxygen and yttrium vacancies. Here, V_O defects present

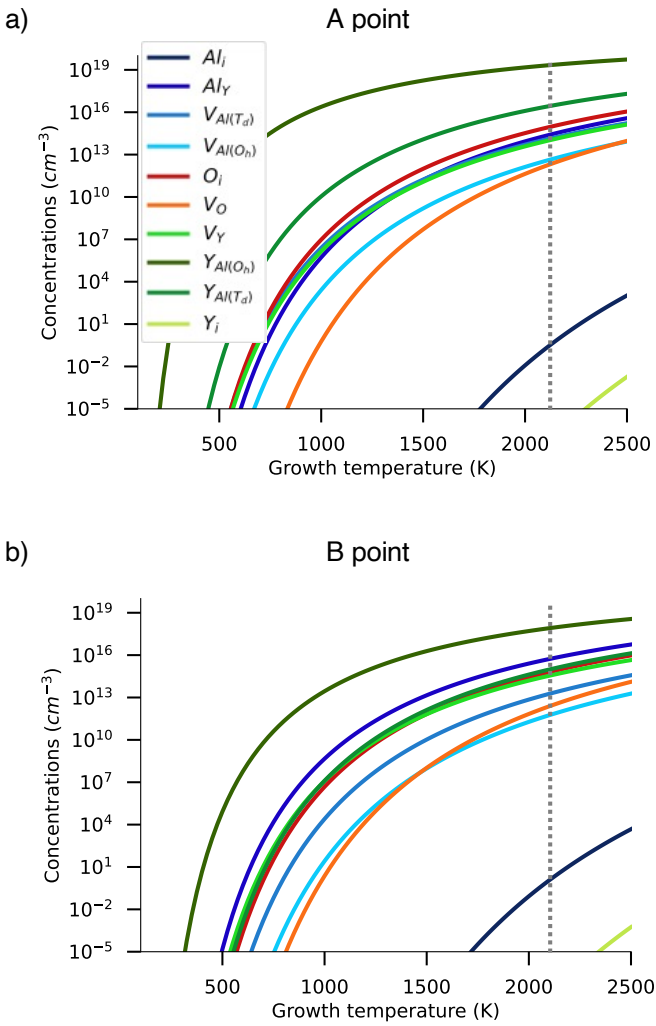

Fig. 6 Defect concentrations *vs* the growth temperature for the O-rich synthesis condition at the a) A and b) B points. T_{gr} = 1850 °C is evidenced by a grey dotted line.

very low DFEs at about 1.4 eV for $q = 0$, slightly lower than $Y_{Al(O_h)}$ species (1.7 eV, as for the B point, both located at the Al_2O_3 border). As reported in Figure 7a, for T_{gr} = 1850 °C (E_F^{gr} = 4.3 eV), the oxygen vacancies are more easily formed (above 10^{19} cm^{-3}) compared to $Y_{Al(O_h)}$ (below 10^{18} cm^{-3}), Al_Y ($\sim 10^{16}$ cm^{-3}), etc. In case of the O-poor E point (see Figure 4b), DFEs for

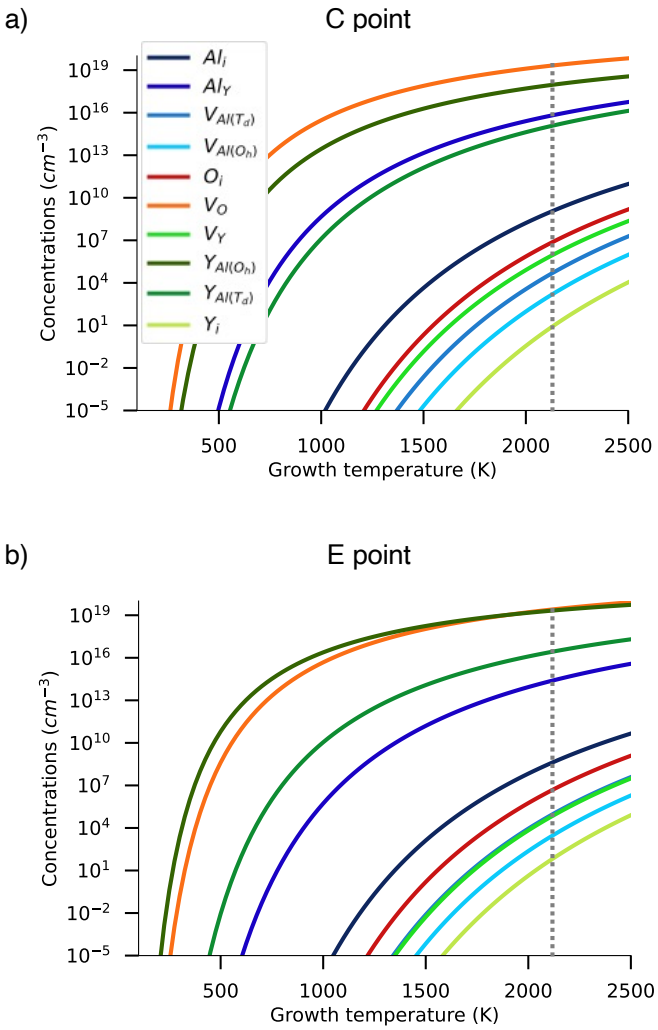

Fig. 7 Defect concentrations *vs* the growth temperature for the O-poor synthesis condition at the a) C and b) E points. T_{gr} = 1850 °C is evidenced by a grey dotted line.

$Y_{Al(O_h)}$ defects decrease down to 1.17 eV, while the ones for V_O were computed nearby 1.40 eV. For T_{gr} = 1850 °C (see Figure 7b), E_F^{gr} does not change compared to the C point, and the higher concentrations were estimated for the $Y_{Al(O_h)}$ and V_O defects (above 10^{19} cm^{-3}), far from the others (below 10^{16} cm^{-3} for $Y_{Al(T_d)}$, Al_Y, etc.). These results confirm previous work at the LDA level [40] and highlight the fact that i) oxygen vacancies are favoured

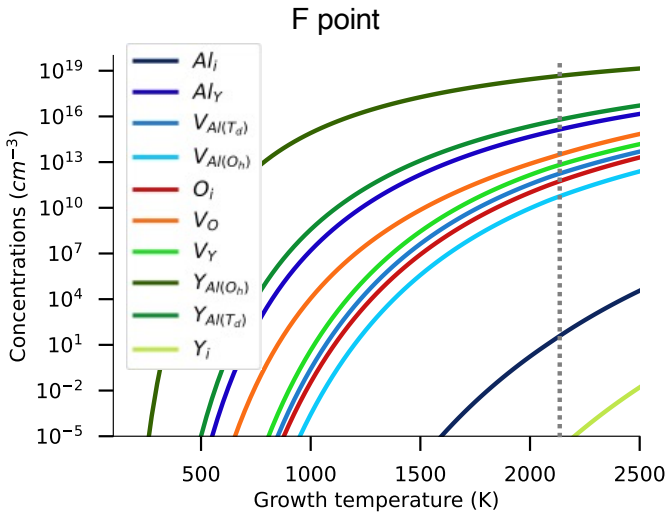

Fig. 8 Defect concentrations *vs* the growth temperature for the O-intermediate synthesis condition at the F point. T_{gr} = 1850 °C is evidenced by a grey dotted line.

in O-poor conditions and ii) the substitution of Al(O_h) by Y can be limited by performing synthesis near the Al_2O_3-rich (C point) limit even under these reducing atmospheres.

For the intermediate conditions defined by the F point (see Figure 5), the dopability domain is set between 1.89 and 5.16 eV by the same vacancies. The $Y_{Al(O_h)}$ entities show (again) the lowest DFEs (1.40 eV) for most available μ_{E_F} values, while the highest DFEs are found for interstitial cations. For T_{gr} = 1850 °C (E_F^{gr} = 3.85 eV (see Figure 8), we still demonstrated that, as expected, $Y_{Al(O_h)}$ show higher concentrations (above 10^{18} cm^{-3}) than the others computed below ~10^{15} cm^{-3} as $Y_{Al(T_d)}$, Al_Y, etc.

Regarding the charge transition levels (see SI Table S4), their positions with respect to the band gap are depicted in Figure 9a. All cation vacancies present defect levels located far from the VBM between roughly 1.5 and 2.5 eV. Oxygen vacancies were found to create deep transition levels at the middle of the band gap between 2.6 and 3.1 eV from the CBM, confirming the deep traps already

reported in theoretical and experimental investigations [19, 41–44]. Regarding interstitials, Al_i and Y_i species introduce relatively deep levels between ∼1.1 and 2.2 eV from the CBM, while deep levels of oxygen species are found around 2.5 and 3.5 eV above the VBM. In case of cationic antisites, neutral defects are stabilized in the overall of the band gap, the first charge transition levels being located near band edges agreeing very well with already published studies [19, 45]. Thus, whatever the synthesis conditions are, $Y_{Al(O_h)}$ species are present at the charge state $q = 0$, leading to formally Y^{3+} cations that may occupy 16*a* sites. More specifically to O-poor conditions, the oxygen vacancies also exist at $q = 0$, *i.e.* oxygen vacancies doubly occupied by electrons.

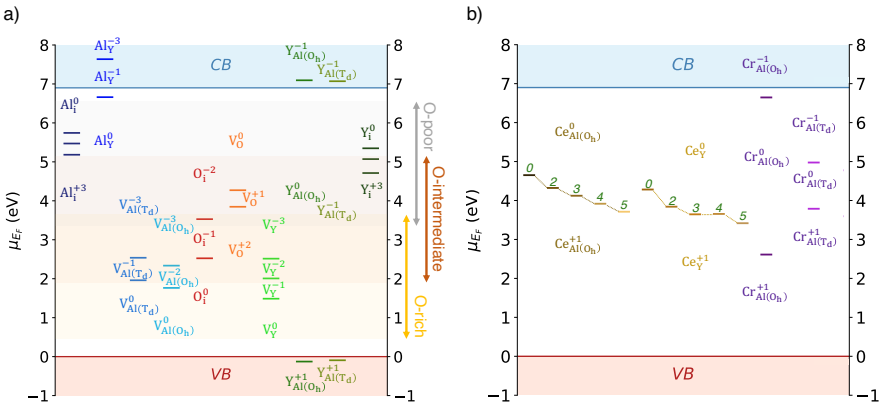

Fig. 9 Position of charge transition levels for each a) intrinsic and b) extrinsic defect species. Regarding transition levels determined for Ce-based defects, the U_{eff} Hubbard values set for Ce-4*f* orbitals (*i.e.* 0, 2, 3, 4 and 5 eV) are indicated in green above the associated levels. The arrows represent the limits of the dopability domains in O-poor (grey), O-intermediate (red) and O-rich (yellow) conditions.

Briefly, we showed that the presence of Y in Al(O_h) sites (*i.e.* antisites $Y_{Al(O_h)}$) cannot be avoided during the crystal growth, whatever the synthesis conditions are, and their concentrations are always relatively important at high temperatures of synthesis (see SI Table S5). More specifically to reducing conditions, the formation of oxygen vacancies can compete with the creation of $Y_{Al(O_h)}$ species and produce deep traps within the band gap in contrast

with $\epsilon\,(0/+1)$ and $\epsilon\,(-1/0)$ levels located within the valence and conduction bands, respectively.

After clarifying the impact of native point defects on the electronic structure of the YAG compound, we focus our attention on commonly encountered extrinsic dopants which substitute yttrium or aluminium atoms, namely i) cerium (Ce) for which activated Ce^{3+} cation enables the emergence of luminescent properties, and ii) chromium (Cr) supposed to favour the persistent luminescence by introducing shallow Cr^{3+}/Cr^{2+} electron traps near the CBM [46]. Hereafter, our main interest is devoted to determining the positions of charge transition levels induced by the insertion of Ce and Cr in YAG. The laters ones are independent of the synthesis conditions. The impact of Ga substitution is out of the scope of our discussion. Namely, Ga at Al sites as dopant would not induce extra defect levels within the gap of YAG, but the substitution of Al by Ga at higher substituting level triggers a decrease of the optical gap with the aforementioned stabilization in energy of the CBM. Such lowering of the CBM appears of prior importance to get access to electron traps and enable persistent luminescence of co-doped YAG:Ce,Cr at room temperature [18, 47].

3.2 Ce doping

YAG:Ce^{3+} is a widely encountered phosphor which exhibits a $5d$-$4f$ yellowish emission at ≈550 nm when excited by a light of 430-450 nm [48–50]. The position of the Ce^{3+} ground state within the band gap has been reported at ∼3.8 eV below the CBM and the Ce-$5d$ orbitals near the CBM [4, 51–54]. Here, we assess the ability of our approach to determine the location of the Ce^{3+}/Ce^{4+} transition level for substituting dopants.

Regarding the nature of defects, the literature commonly presents the preferential substitution of yttrium by cerium (labelled Ce_Y) [12], notably on the basis of their close ionic Shannon radii (r = 1.159 Å for yttrium, r = 1.283 Å for cerium) when both Y^{3+} and Ce^{3+} species are located at 8-coordinated sites. We examined the expected substitution Ce_Y, and also the possibility to observe Ce at octahedral aluminium sites (labelled $Ce_{Al(O_h)}$). The U_{eff} Hubbard correction applied on Ce-4f states was varied in a reasonable 0-5 eV range. The new stability domains established with Ce-based competing phases (see SI Table S6) are detailed for several Hubbard values in SI Table S7-11. One may notably retrieve among them the previously found A and B O-rich points (hereafter labelled A' and B') which are now also limited by the CeO_2 phase, while the C', D' and E' points are now also set by the $CeAl_3$ phase. The charge transition levels (see Figure 9 and SI Table S12) were estimated from DFEs determined under an O-poor atmosphere (the C' point, see SI Table S7) only and shown for U_{eff} = 0 (*i.e.* no Hubbard correction) and 5 eV in Figure 10.

In brief, DFEs obtained for the C' atmosphere reveal that Ce_Y entities are preferentially created compared to the $Ce_{Al(O_h)}$ ones, whatever the value of the Hubbard correction is. Typically, for U_{eff} = 0 eV, DFEs for q = 0 were found at 1.21 and 3.53 eV for Ce^0_Y and $Ce^0_{Al(O_h)}$, respectively. For U_{eff} = 5 eV, the same quantities were respectively estimated at 0.32 and 2.84 eV.

The analysis of DFEs also demonstrates that in case that such species would be formed, Ce^{3+} defects would predominantly exist within the overall of the dopability domain set by V_O and V_Y. Also, the $\epsilon(0/+1)$ levels (*i.e.* the $4f_1$ block of Ce^{3+}) are located nearby the middle of the band gap. More precisely, the levels for $Ce_{Al(O_h)}$ entities, never calculated before to our knowledge, were computed at 2.25, 2.58 and 3.19 eV from the CBM for U_{eff} = 0, 2 and 5 eV, respectively (see Figure 9b). For Ce_Y species, these levels would be situated at

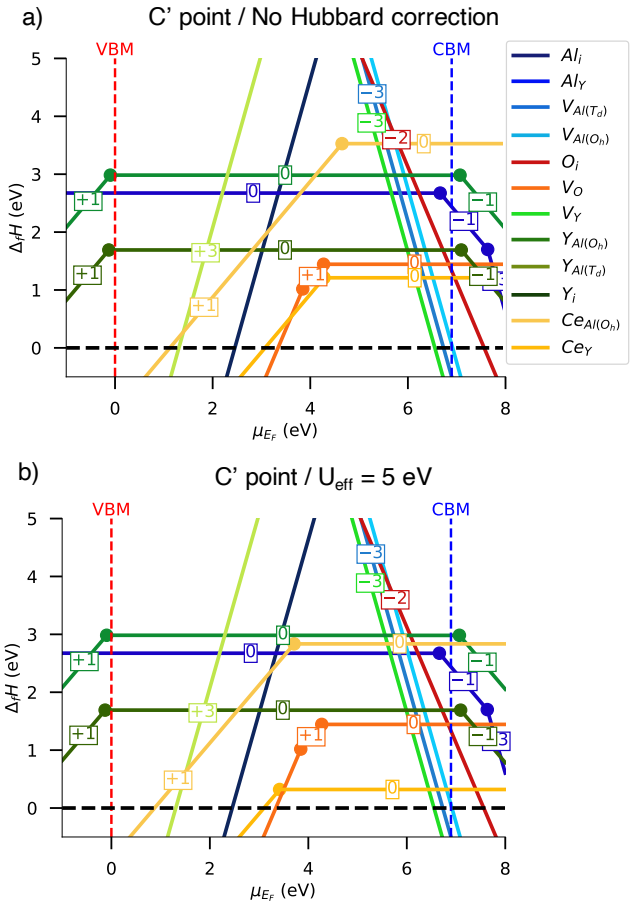

Fig. 10 Defect formation enthalpies *vs* the Fermi level for Ce-doping under C' O-poor atmosphere for (a) $U_{eff} = 0$ eV and (b) $U_{eff} = 5$ eV.

2.62, 3.06 and 3.48 eV below the CBM, respectively. Taking into account the fact that DFEs are significantly lower for Ce_Y than $Ce_{Al(O_h)}$, one may confirm that the experimental level found at ∼3.8 eV below the CBM [4, 51–53] is attributed to Ce located in Y sites. By increasing the U_{eff} term up to 5 eV, the Ce-4f states are located deeper in energy, and the simulated formal Ce^{3+}/Ce^{4+} level is getting closer to the experiment (the d orbitals are not affected by the U_{eff} term applied only on 4f, and are positioned just below the CBM). Thus, one may conclude that a more reliable description of the electronic properties

of Ce-based defects in YAG is reached with high U_{eff} parameters, in contrast to the theoretical value of 2 eV reported in the literature [30].

3.3 Cr doping

Chromium is encountered at the oxidation state +III and +IV when used as (co)dopant in YAG [55–59]. Also, Ueda *et al.* [14, 15] reported that Cr^{3+} species actively participate to the enhancement of the persistent luminescence in YAG:Ce,Cr by introducing shallow electron traps located at 0.6-1 eV from the CBM [46, 60]. We took the opportunity of this study to re-investigate the position of both Cr^{2+}/Cr^{3+} and Cr^{3+}/Cr^{4+} transition levels.

Herein, we considered the substitution of Al positioned in tetrahedral and octahedral sites, respectively labelled $Cr_{Al(T_d)}$ and $Cr_{Al(O_h)}$. The stability domain of YAG phase was investigated taking into account five Cr-based competitive phases (see SI Table S13). Eleven extreme limits were extracted (see Table S14). Here, Cr_2O_3 and Y_2AlCrO_6 are new competitive phases under previous A and B O-rich conditions (now labelled A" and B"), while the $AlCr_2$ compound is now limiting at the C", D" and E" O-poor points. Hereafter, we focus on the G" O-poor atmosphere (see SI Table S13) for which Cr-based defects are more easily created than in C" and at which the formation of Cr, Y_2O_3 and $AlCr_2$ is competing with YAG. DFEs were calculated and shown in Figure 11. The charge transition levels for all point defects are schematically summed up in Figure 9b and reported in SI Table S15.

DFEs decrease going from $Cr^0_{Al(T_d)}$ species (3.30 eV) to $Cr^0_{Al(T_d)}$ ones (1.97 eV). Consequently, $Cr_{Al(O_h)}$ entities appear as the predominant Cr-based defect for most of μ_{E_F} values, which lets us suggest the preferential occupation of Al octahedral sites by Cr, that chemically speaking is reasonable.

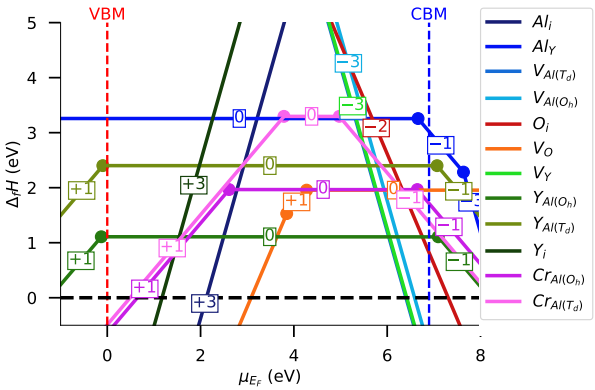

Fig. 11 Defect formation enthalpies *vs* the Fermi level for Cr-doping under G" O-poor atmosphere.

The charge transition levels $\epsilon\,(-1/0)$ (*i.e.* formally Cr^{2+}/Cr^{3+} redox potential) and $\epsilon\,(0/+1)$ (*i.e.* formally Cr^{3+}/Cr^{4+} redox potential) were determined on the basis of DFEs and are respectively positioned at 4.98 eV and 3.79 eV for $Cr_{Al(T_d)}$ defects. Those transition levels were found deep in the band gap (1.92 eV and 3.11 eV below the CBM, respectively), and are thus not supposed to be responsible for the observed persistent luminescence in doped YAG. Concerning $Cr_{Al(O_h)}$ defects, the $\epsilon\,(-1/0)$ and $\epsilon\,(0/+1)$ defect levels were respectively assessed at 2.61 and 6.65 eV as seen in Figure 11. In this situation, electron traps related to Cr^{2+}/Cr^{3+} levels are located near the CBM at 0.25 eV, not so far from the experimental 0.8 eV value [18]. This energy could be reasonably associated to the detrapping energy needed to account for the observed luminescent features in persistent luminescence in (Ce^{3+},Cr^{3+}) doped YAG from thermoluminescence glow curves. This energy would correspond to the process $Cr^{2+} \rightarrow Cr^{3+} + e^-$, the released electron recombining at the photoionized Ce site via the CBM according to the reaction $Ce^{4+} + e^- \rightarrow Ce^{3+}$. One can notice here that Al_Y antisites with a $\epsilon\,(-1/0)$ defect level at 0.24 eV might also play the role of electron traps in the features of persistent luminescence garnets.

4 Conclusion

Theoretical investigations have been performed at the SCAN DFT level to simulate point defects into YAG. Based on the analysis of the stability diagram of the host compound, different possible synthesis conditions have been identified. We have notably shown that antisite defects always exist in significant concentrations and cannot be avoided during the synthesis. Under O-poor atmosphere, oxygen vacancies can constitute the predominant defect and create charge carrier traps at the middle of the gap.

Also, we investigated the substitution of cations by dopants, namely Ce and Cr. Our findings enable to access the position of charge transition levels and explain experimental measurements. For cerium-based defects, one evidenced that increasing the Hubbard correction up to 5 eV (at minimum) enables to recover Ce^{3+}/Ce^{4+} transition level near experiments. Also, our simulations nicely reproduce the presence of electron traps from chromium species close to the CBM.

In the near future, it would be interesting to perform such computations using a more refined model to be even more accurate, for instance including proper treatments for spin-orbit and relativistic effects. Furthermore, one may use hybrid functional for the whole study that would prevent corrections on the band-edges and, consequently, induce a better localization of the charge transition levels. However, one should mention that inclusion of all these corrections would dramatically rise the computational time by several orders of magnitude.

Supplementary information. More details on corrections for the estimation of defect formation enthalpies, method used to estimate defect concentrations, stability domains of the YAG phase during syntheses, initial position of interstitials, representation of the initial interstitial positions.

Acknowledgments. This work was granted access to the HPC resources of TGCC under allocation 2020-A0080911491 and A0090912034 made by GENCI. W.L.-D.-H. particularly thanks the financial support by the ANR-18-CE08-0012 PERSIST project of the French National Research Agency and the CNRS.

References

[1] Slack, G.A., Oliver, D.W., Chrenko, R.M., Roberts, S.: Optical Absorption of $Y_3Al_5O_{12}$ from 10- to 55 000 cm^{-1} Wave Numbers. Physical Review **177**(3), 1308–1314 (1969). https://doi.org/10.1103/PhysRev.177.1308. Accessed 2020-07-07

[2] Murk, V., Yaroshevich, N.: Exciton and recombination processes in YAG crystals. Journal of Physics: Condensed Matter **7**(29), 5857–5864 (1995). https://doi.org/10.1088/0953-8984/7/29/012. Accessed 2021-02-25

[3] Jain, A., Sengar, P., Hirata, G.A.: Rare-earth-doped $Y_3Al_5O_{12}$ (YAG) nanophosphors: synthesis, surface functionalization, and applications in thermoluminescence dosimetry and nanomedicine. Journal of Physics D: Applied Physics **51**(30), 303002 (2018). https://doi.org/10.1088/1361-6463/aaca49. Accessed 2020-07-25

[4] Dorenbos, P.: Electronic structure and optical properties of the lanthanide activated $RE_3(Al_{1-x}Ga_x)_5O_{12}$ (RE = Gd, Y, Lu) garnet compounds. Journal of Luminescence **134**, 310–318 (2013). https://doi.org/10.1016/j.jlumin.2012.08.028. Accessed 2020-10-30

[5] Geusic, J.E., Marcos, H.M., Van Uitert, L.G.: Laser oscillations in Nd-doped yttrium aluminium, yttrium gallium and gadolinium garnets.

Applied Physics Letters **4**(10), 182–184 (1964). https://doi.org/10.1063/1.1753928. Accessed 2020-07-12

[6] Kurtz, R., Fathe, L., Machan, J., Birnbaum, M.: Multiple Wavelength Lasing of (Er,Ho):YAG. In: Advanced Solid State Lasers, p. 6. Optical Society of America, ??? (1989). https://doi.org/10.1364/ASSL.1989.DD6. Journal Abbreviation: Advanced Solid State Lasers. http://www.osapublishing.org/abstract.cfm?URI=ASSL-1989-DD6

[7] Lupei, V., Lupei, A.: Nd:YAG at its 50th anniversary: Still to learn. Journal of Luminescence **169**, 426–439 (2016). https://doi.org/10.1016/j.jlumin.2015.04.018. Accessed 2020-07-12

[8] Gautam, G.D., Pandey, A.K.: Pulsed Nd:YAG laser beam drilling: A review. Optics & Laser Technology **100**, 183–215 (2018). https://doi.org/10.1016/j.optlastec.2017.09.054. Accessed 2020-02-10

[9] Autrata, R., Schauer, P., Kuapil, J., Kuapil, J.: A single crystal of YAG-new fast scintillator in SEM. Journal of Physics E: Scientific Instruments **11**(7), 707–708 (1978). https://doi.org/10.1088/0022-3735/11/7/028. Accessed 2020-07-12

[10] Jüstel, T., Nikol, H., Ronda, C.: New Developments in the Field of Luminescent Materials for Lighting and Displays. Angewandte Chemie International Edition **37**(22), 3084–3103 (1998). https://doi.org/10.1002/(SICI)1521-3773(19981204)37:22⟨3084::AID-ANIE3084⟩3.0.CO;2-W. Accessed 2020-07-25

[11] Xia, Z., Meijerink, A.: Ce^{3+}-Doped garnet phosphors: composition modification, luminescence properties and applications. Chemical Society

Reviews **46**(1), 275–299 (2017). https://doi.org/10.1039/C6CS00551A. Accessed 2020-07-12

[12] Ueda, J., Tanabe, S.: Review of luminescent properties of Ce^{3+}-doped garnet phosphors: New insight into the effect of crystal and electronic structure. Optical Materials: X **1**, 100018 (2019). https://doi.org/10.1016/j.omx.2019.100018. Accessed 2020-10-08

[13] Berends, A.C., van de Haar, M.A., Krames, M.R.: YAG:Ce^{3+} Phosphor: From Micron-Sized Workhorse for General Lighting to a Bright Future on the Nanoscale. Chemical Reviews **120**(24), 13461–13479 (2020). https://doi.org/10.1021/acs.chemrev.0c00618. Accessed 2021-02-02

[14] Ueda, J., Kuroishi, K., Tanabe, S.: Bright persistent ceramic phosphors of Ce^{3+}-Cr^{3+}-codoped garnet able to store by blue light. Applied Physics Letters **104**(10), 101904 (2014). https://doi.org/10.1063/1.4868138. Accessed 2020-07-01

[15] Ueda, J., Dorenbos, P., Bos, A.J.J., Kuroishi, K., Tanabe, S.: Control of electron transfer between Ce^{3+} and Cr^{3+} in the $Y_3Al_{5-x}Ga_xO_{12}$ host via conduction band engineering. Journal of Materials Chemistry C **3**(22), 5642–5651 (2015). https://doi.org/10.1039/C5TC00546A. Accessed 2021-04-23

[16] Ching, W.Y., Xu, Y.-N., Brickeen, B.K.: Ab-initio calculation of excited state absorption of Cr^{4+} in $Y_3Al_5O_{12}$. Applied Physics Letters **74**(25), 3755–3757 (1999). https://doi.org/10.1063/1.124170. Accessed 2020-07-13

[17] Muñoz-García, A.B., Seijo, L.: Structural, electronic, and spectroscopic

effects of Ga codoping on Ce-doped yttrium aluminum garnet: First-principles study. Physical Review B **82**(18), 184118 (2010). https://doi.org/10.1103/PhysRevB.82.184118. Accessed 2020-10-30

[18] Muñoz-García, A.B., Barandiarán, Z., Seijo, L.: Antisite defects in Ce-doped YAG ($Y_3Al_5O_{12}$): first-principles study on structures and 4f–5d transitions. Journal of Materials Chemistry **22**(37), 19888–19897 (2012). https://doi.org/10.1039/C2JM34479C. Accessed 2020-01-15

[19] Linderälv, C., Åberg, D., Erhart, P.: Luminescence Quenching via Deep Defect States: A Recombination Pathway via Oxygen Vacancies in Ce-Doped YAG. Chemistry of Materials **33**(1), 73–80 (2021). https://doi.org/10.1021/acs.chemmater.0c02449. Accessed 2021-02-02

[20] Miyamoto, Y., Nakamura, H., Akai, T.: Franck-Condon relaxation in photo-excited YAG:Ce studied using real-time time-dependent density functional theory. Journal of Luminescence **229**, 117647 (2021). https://doi.org/10.1016/j.jlumin.2020.117647. Accessed 2021-02-02

[21] Kresse, G., Furthmüller, J.: Efficiency of ab-initio total energy calculations for metals and semiconductors using a plane-wave basis set. Computational Materials Science **6**(1), 15–50 (1996). https://doi.org/10.1016/0927-0256(96)00008-0. Accessed 2020-01-24

[22] Kresse, G., Furthmüller, J.: Efficient iterative schemes for ab initio total-energy calculations using a plane-wave basis set. Physical Review B **54**(16), 11169–11186 (1996). https://doi.org/10.1103/PhysRevB.54.11169. Accessed 2020-01-24

[23] Kresse, G., Joubert, D.: From ultrasoft pseudopotentials to the projector

augmented-wave method. Physical Review B **59**(3), 1758–1775 (1999). https://doi.org/10.1103/PhysRevB.59.1758. Accessed 2020-01-24

[24] Sun, J., Ruzsinszky, A., Perdew, J.: Strongly Constrained and Appropriately Normed Semilocal Density Functional. Physical Review Letters **115**(3), 036402 (2015). https://doi.org/10.1103/PhysRevLett.115.036402. Accessed 2020-01-24

[25] Euler, F., Bruce, J.A.: Oxygen coordinates of compounds with garnet structure. Acta Crystallographica **19**(6), 971–978 (1965). https://doi.org/10.1107/S0365110X65004747. Accessed 2020-07-07

[26] Ning, L., Ji, X., Dong, Y., Jin, W., Huang, Y., Pan, Z., Tanner, P.A.: First-principles study of Ce-doped $Y_3Al_5O_{12}$ with Si–N incorporation: electronic structures and optical properties. Journal of Materials Chemistry C **4**(23), 5214–5221 (2016). https://doi.org/10.1039/C6TC01691J. Accessed 2020-01-15

[27] Adamo, C., Barone, V.: Toward reliable density functional methods without adjustable parameters: The PBE0 model. The Journal of Chemical Physics **110**(13), 6158–6170 (1999). https://doi.org/10.1063/1.478522. Accessed 2022-05-08

[28] Stoliaroff, A., Latouche, C.: Accurate Ab Initio Calculations on Various PV-Based Materials: Which Functional to Be Used? The Journal of Physical Chemistry C **124**(16), 8467–8478 (2020). https://doi.org/10.1021/acs.jpcc.9b10821. Accessed 2020-08-26

[29] Long, O.Y., Sai Gautam, G., Carter, E.A.: Evaluating optimal u

for 3*d* transition-metal oxides within the SCAN+*u* framework. Physical Review Materials **4**(4), 045401 (2020). https://doi.org/10.1103/PhysRevMaterials.4.045401. Accessed 2020-04-12

[30] Sai Gautam, G., Carter, E.A.: Evaluating transition metal oxides within DFT-SCAN and SCAN+U frameworks for solar thermochemical applications. Physical Review Materials **2**(9), 095401 (2018). https://doi.org/10.1103/PhysRevMaterials.2.095401. Accessed 2020-04-12

[31] Dudarev, S.L., Botton, G.A., Savrasov, S.Y., Humphreys, C.J., Sutton, A.P.: Electron-energy-loss spectra and the structural stability of nickel oxide: An LSDA+U study. Physical Review B **57**(3), 1505–1509 (1998). https://doi.org/10.1103/PhysRevB.57.1505. Accessed 2020-02-03

[32] Péan, E., Vidal, J., Jobic, S., Latouche, C.: Presentation of the PyDEF post-treatment Python software to compute publishable charts for defect energy formation. Chemical Physics Letters **671**, 124–130 (2017). https://doi.org/10.1016/j.cplett.2017.01.001. Accessed 2020-03-25

[33] Stoliaroff, A., Jobic, S., Latouche, C.: PyDEF 2.0: An Easy to Use Post-treatment Software for Publishable Charts Featuring a Graphical User Interface. Journal of Computational Chemistry **39**(26), 2251–2261 (2018). https://doi.org/10.1002/jcc.25543. Accessed 2020-02-20

[34] Zhang, S.B., Northrup, J.E.: Chemical potential dependence of defect formation energies in GaAs: Application to Ga self-diffusion. Physical Review Letters **67**(17), 2339–2342 (1991). https://doi.org/10.1103/PhysRevLett.67.2339. Accessed 2022-07-04

[35] Stoliaroff, A., Jobic, S., Latouche, C.: New insights into the determination

of maximum chemical potentials to account for alkali doping in β-In_2S_3 by ab initio calculations. Computational Materials Science **168**, 221–228 (2019). https://doi.org/10.1016/j.commatsci.2019.06.011. Accessed 2020-02-20

[36] Kuklja, M.M.: Defects in yttrium aluminium perovskite and garnet crystals: atomistic study. Journal of Physics: Condensed Matter **12**(13), 2953–2967 (2000). https://doi.org/10.1088/0953-8984/12/13/307. Accessed 2020-05-31

[37] Donnerberg, H., Catlow, C.R.A.: Atomistic computer simulations of yttrium iron garnet (YIG) as an approach to materials defect chemistry. I. Intrinsic defects. Journal of Physics: Condensed Matter **5**(18), 2947–2960 (1993). https://doi.org/10.1088/0953-8984/5/18/017. Accessed 2020-07-13

[38] Stanek, C.R., McClellan, K.J., Levy, M.R., Milanese, C., Grimes, R.W.: The effect of intrinsic defects on $RE_3Al_5O_{12}$ garnet scintillator performance. Nuclear Instruments and Methods in Physics Research Section A: Accelerators, Spectrometers, Detectors and Associated Equipment **579**(1), 27–30 (2007). https://doi.org/10.1016/j.nima.2007.04.006. Accessed 2020-07-12

[39] Liu, B., Gu, M., Liu, X., Huang, S., Ni, C.: Formation energies of antisite defects in $Y_3Al_5O_{12}$: A first-principles study. Applied Physics Letters **94**(12), 121910 (2009). https://doi.org/10.1063/1.3109799. Accessed 2020-02-10

[40] Li, Z., Liu, B., Wang, J., Sun, L., Wang, J., Zhou, Y.: Mechanism of Intrinsic Point Defects and Oxygen Diffusion in Yttrium Aluminum Garnet:

First-Principles Investigation. Journal of the American Ceramic Society **95**(11), 3628–3633 (2012). https://doi.org/10.1111/j.1551-2916.2012.05440.x. Accessed 2020-05-31

[41] Chen, J., Lu, T.C., Xu, Y., Xu, A.G., Chen, D.Q.: Ab initio study of a charged vacancy in yttrium aluminum garnet ($Y_3Al_5O_{12}$). Journal of Physics: Condensed Matter **20**(32), 325212 (2008). https://doi.org/10.1088/0953-8984/20/32/325212. Accessed 2020-05-31

[42] Chen, J., Xu, Y., Chen, D.-q.: First-principle calculations on color center in Y–Al–O system. Nuclear Instruments and Methods in Physics Research Section B: Beam Interactions with Materials and Atoms **267**(18), 3028–3031 (2009). https://doi.org/10.1016/j.nimb.2009.06.052. Accessed 2020-02-10

[43] Varney, C.R., Mackay, D.T., Pratt, A., Reda, S.M., Selim, F.A.: Energy levels of exciton traps in yttrium aluminum garnet single crystals. Journal of Applied Physics **111**(6), 063505 (2012). https://doi.org/10.1063/1.3693581. Accessed 2020-07-01

[44] Marinopoulos, A.G.: First-principles study of the formation energies and positron lifetimes of vacancies in the Yttrium-Aluminum Garnet $Y_3Al_5O_{12}$. The European Physical Journal B **92**(11), 242 (2019). https://doi.org/10.1140/epjb/e2019-100392-0. Accessed 2020-01-15

[45] Zorenko, Y., Voloshinovskii, A., Konstankevych, I., Kolobanov, V., Mikhailin, V., Spassky, D.: Luminescence of excitons and antisite defects in the phosphors based on garnet compounds. Radiation Measurements **38**(4), 677–680 (2004). https://doi.org/10.1016/j.radmeas.2004.02.009. Accessed 2020-07-13

[46] Ueda, J., Hashimoto, A., Takemura, S., Ogasawara, K., Dorenbos, P., Tanabe, S.: Vacuum referred binding energy of 3d transition metal ions for persistent and photostimulated luminescence phosphors of cerium-doped garnets. Journal of Luminescence **192**, 371–375 (2017). https://doi.org/10.1016/j.jlumin.2017.07.006. Accessed 2020-10-08

[47] Ueda, J.: Analysis of optoelectronic properties and development of new persistent phosphor in Ce^{3+}-doped garnet ceramics. Journal of the Ceramic Society of Japan **123**(1444), 1059–1064 (2015). https://doi.org/10.2109/jcersj2.123.1059

[48] Wong, C.M., Rotman, S.R., Warde, C.: Optical studies of cerium doped yttrium aluminum garnet single crystals. Applied Physics Letters **44**(11), 1038–1040 (1984). https://doi.org/10.1063/1.94629. Accessed 2020-07-12

[49] Rotman, S.R., Tuller, H.L., Warde, C.: Defect-property correlations in garnet crystals. VI. The electrical conductivity, defect structure, and optical properties of luminescent calcium and cerium-doped yttrium aluminum garnet. Journal of Applied Physics **71**(3), 1209–1214 (1992). https://doi.org/10.1063/1.351289. Accessed 2020-07-14

[50] Zych, E., Brecher, C., Glodo, J.: Kinetics of cerium emission in a YAG:Ce single crystal: the role of traps. Journal of Physics: Condensed Matter **12**(8), 1947–1958 (2000). https://doi.org/10.1088/0953-8984/12/8/336. Accessed 2020-07-13

[51] Pedrini, C., Rogemond, F., McClure, D.S.: Photoionization thresholds of rare-earth impurity ions. Eu^{2+}:CaF_2, Ce^{3+}:YAG, and Sm^{2+}:CaF_2. Journal of Applied Physics **59**(4), 1196–1201 (1986). https://doi.org/10.1063/1.336557. Accessed 2021-02-26

[52] Hamilton, D.S., Gayen, S.K., Pogatshnik, G.J., Ghen, R.D., Miniscalco, W.J.: Optical-absorption and photoionization measurements from the excited states of Ce^{3+}:$Y_3Al_5O_{12}$. Physical Review B **39**(13), 8807–8815 (1989). https://doi.org/10.1103/PhysRevB.39.8807. Accessed 2021-02-26

[53] Ueda, J., Tanabe, S., Nakanishi, T.: Analysis of Ce^{3+} luminescence quenching in solid solutions between $Y_3Al_5O_{12}$ and $Y_3Ga_5O_{12}$ by temperature dependence of photoconductivity measurement. Journal of Applied Physics **110**(5), 053102 (2011). https://doi.org/10.1063/1.3632069. Accessed 2020-11-13

[54] Ueda, J., Dorenbos, P., Bos, A.J.J., Meijerink, A., Tanabe, S.: Insight into the Thermal Quenching Mechanism for $Y_3Al_5O_{12}$:Ce^{3+} through Thermoluminescence Excitation Spectroscopy. The Journal of Physical Chemistry C **119**(44), 25003–25008 (2015). https://doi.org/10.1021/acs.jpcc.5b08828. Accessed 2020-11-13

[55] Eichler, H.J., Haase, A., Kokta, M.R., Menzel, R.: Cr^{4+}:YAG as passive Q-switch for a Nd:YALO oscillator with an average repetition rate of 2.7 kHz, TEM00 mode and 13 W output. Applied Physics B **58**(5), 409–411 (1994). https://doi.org/10.1007/BF01081882. Accessed 2020-10-30

[56] Grinberg, M., Sikorska, A., Śliwiński, A., Barzowska, J., Shen, Y.R., Ubizskii, S.B., Melnyk, S.S.: Photoacoustic and optical absorption spectroscopy studies of luminescent Cr^{3+} and Cr^{4+} centers in yttrium aluminum garnet. Physical Review B **67**(4), 045113 (2003). https://doi.org/10.1103/PhysRevB.67.045113. Accessed 2020-07-14

[57] Kinsman, K.M., McKittrick, J., Sluzky, E., Hesse, K.: Phase Development and Luminescence in Chromium-Doped Yttrium Aluminum Garnet

(YAG:Cr) Phosphors. Journal of the American Ceramic Society **77**(11), 2866–2872 (1994). https://doi.org/10.1111/j.1151-2916.1994.tb04516.x. Accessed 2020-07-14

[58] Ayvacikli, M., Canimoglu, A., Muresan, L.E., Barbu Tudoran, L., Garcia Guinea, J., Karabulut, Y., Jorge, A., Karali, T., Can, N.: Structural and luminescence effects of Ga co-doping on Ce-doped yttrium aluminate based phosphors. Journal of Alloys and Compounds **666**, 447–453 (2016). https://doi.org/10.1016/j.jallcom.2016.01.113. Accessed 2020-10-30

[59] Bagdasarov, K.S., Pasternak, L.B., Sevast'yanov, B.K.: Radiation color centers in $Y_3Al_5O_{12}$:Cr^{3+} crystals. Soviet Journal of Quantum Electronics **7**(8), 965 (1977). https://doi.org/10.1070/QE1977v007n08ABEH012694. Accessed 2020-07-12

[60] Chen, D., Zhou, Y., Xu, W., Zhong, J., Huang, P.: Persistent and photo-stimulated luminescence in Ce^{3+}/Cr^{3+} activated $Y_3Al_2Ga_3O_{12}$ phosphors and transparent phosphor-in-glass. Journal of Materials Chemistry C **4**(48), 11457–11464 (2016). https://doi.org/10.1039/C6TC04140J. Accessed 2020-09-03